

Wide-field spatio-spectral interferometry: theory and imaging properties

ALEXANDER S. IACCHETTA* AND JAMES R. FIENUP

Institute of Optics, Univ. of Rochester, 275 Hutchison Rd., Rochester, New York 14627-0186, USA

*Corresponding author: alexander.iacchetta@gmail.com

Received 16 June 2017; revised 21 August 2017; accepted 29 August 2017; posted 29 August 2017 (Doc. ID 298266); published 22 September 2017

The emerging astronomical technique known as wide-field spatio-spectral interferometry can provide hyperspectral images with spatial resolutions that are unattainable with a single monolithic-aperture observatory. The theoretical groundwork for operation and data measurement is presented in full detail, including relevant coherence theory. We also discuss a data processing technique for recovering a hyperspectral image from an interferometric data set as well as the unusual effective transfer function of the system. © 2017 Optical Society of America

OCIS codes: (100.3175) Interferometric imaging; (110.3175) Interferometric imaging; (070.0070) Fourier optics and signal processing; (030.0030) Coherence and statistical optics; (110.4234) Multispectral and hyperspectral imaging; (300.6300) Spectroscopy, Fourier transforms.

<https://doi.org/10.1364/JOSAA.34.001896>

1. INTRODUCTION

The theory and method of wide-field spatio-spectral, or double-Fourier, interferometry is intended for spectroscopically imaging extended astronomical objects with a spatial and spectral resolution that, due to cost, weight, and size limitations, cannot be achieved by any single-aperture telescope. This system design can be thought of as a combination of a Michelson stellar interferometer and a Fourier transform imaging spectrometer. Mathematical models for wide-field double-Fourier interferometric imaging have already been developed by Lyon *et al.* [1,2] and by Elias *et al.* [3], who create a more general model that considers polarization effects. The model herein will assume the scalar field approximation, which will resemble the analysis of Lyon *et al.* [1,2]; however, it will address some issues regarding the system's spectral optical transfer function (SOTF), a term introduced by Thurman and Fienup for Fizeau Fourier transform imaging spectroscopy [4,5]. This interpretation will have consequences on image reconstruction and system design. A full derivation of the ideal measurement model is presented in Section 2 with a discussion of sampling considerations and resolution limits in Section 3. The image synthesis algorithm is introduced in Section 4 prior to an examination of the interferometer's imaging properties and limitations, for which we provide some possible solutions, in Section 4.D. Concluding remarks and future work are provided in Section 5. For completeness, connections to coherence theory are provided in Appendix A. Throughout the following derivation, we will consider the case of Fresnel propagation, which will be most pertinent for laboratory experiments but also applies to astronomical imaging as well.

2. MEASUREMENT MODEL

A. Source to Beam Combiner

Before looking into the specifics of the interferometer, we begin by determining the electric field generated by the astronomical sources of interest and propagated to the plane of the interferometer's entrance pupil, having coordinates $\mathbf{x}_{\text{in}} = (x_{\text{in}}, y_{\text{in}})$. We start by considering only a monochromatic point source located at $\boldsymbol{\xi} = (\xi, \eta)$ with wavelength λ . Due to the extremely large distance, z , between the astronomical source and the interferometer, we define the source position by the paraxial approximation for the direction cosines given by the angle with respect to the axis of the interferometer (line perpendicular to the entrance pupil plane of the interferometer that bisects the interferometer apertures and also can be referred to as the line-of-sight) as

$$\boldsymbol{\alpha} = (\alpha, \beta) = -\frac{(\xi, \eta)}{z} = -\frac{\boldsymbol{\xi}}{z}, \quad (1)$$

where the negative sign in the above definition is a matter of sign convention. Note that in a laboratory setting, an effectively large distance, z , is attained by placing the source to be imaged at the focus of collimating optics. In what follows, we will adopt the spectroscopy convention for the scalar wavenumber $\kappa = 1/\lambda = \nu/c$ such that the wavevector is related to the wavenumber and the direction cosines through $\boldsymbol{\kappa} = \kappa\boldsymbol{\alpha}$.

Assuming $E_s(\boldsymbol{\alpha}; \kappa)$ is the field produced by the source at an arbitrary field angle and wavenumber, we can now write the Fresnel approximation, associated with that source field component, for the field incident on the aperture plane of the interferometer at time t as

$$E_{\text{in}}(\mathbf{x}_{\text{in}}, \boldsymbol{\alpha}; \kappa) = \gamma_1 e^{i2\pi\kappa(z-ct)} \exp\left(i\pi \frac{\kappa}{z} \mathbf{x}_{\text{in}}^2\right) E_s(\boldsymbol{\alpha}; \kappa) \times \exp(i\pi\kappa z \boldsymbol{\alpha}^2) \exp(i2\pi\kappa \mathbf{x}_{\text{in}} \cdot \boldsymbol{\alpha}), \quad (2)$$

where

$$\gamma_1 = \frac{iz}{\kappa} \quad (3)$$

and $\boldsymbol{\alpha}^2 = |\boldsymbol{\alpha}|^2$. The time dependence for a monochromatic source is given by a simple time-harmonic relationship, so it is not explicitly included in the list of the above arguments. Without loss of generality, we will reserve the integration over all source angles and all wavenumbers until they are needed for computing intensities. We will eventually be concerned with relative intensity values, so the exact value of γ_1 is not very important, but, for completeness, we will continue to redefine γ_n as new constants appear.

Most astronomical objects are incoherent sources, meaning the fields of all the radiators in the object are uncorrelated; this will be important for simplification later on in the derivation. The presence of spatial or spectral correlation (partial coherence) in the source could induce significant effects, such as, but not limited to, spectral shifting or broadening of the field measured by an interferometer ([6], Section 5.8). The additional considerations of partially coherent and coherent sources would require significant analysis, are unlikely to occur in nature, and will not be discussed any further.

The field just after the entrance pupil plane, having transmittance $A(\mathbf{x}_{\text{in}}; \kappa)$, is given by

$$E_{\text{ap}}(\mathbf{x}_{\text{in}}, \boldsymbol{\alpha}; \kappa) = A(\mathbf{x}_{\text{in}}; \kappa) E_{\text{in}}(\mathbf{x}_{\text{in}}, \boldsymbol{\alpha}; \kappa), \quad (4)$$

where the phase of $A(\mathbf{x}_{\text{in}}; \kappa)$ would be caused by aberrations or other path delays. We assume that the interferometer will have two apertures that are equally displaced about the axis of the interferometer, located in the same plane, and pointed in the same direction. The vector distance between the centers of the apertures is the baseline $\mathbf{B} = (B_x, B_y)$. A simplified diagram of the interferometer is shown in Fig. 1 for a fixed baseline. The two fields just after the equally displaced apertures in the entrance plane of the interferometer are given by

$$E_{1,\text{ap}}(\mathbf{x}_{\text{in}}, \boldsymbol{\alpha}; \kappa) = A_1\left(\mathbf{x}_{\text{in}} - \frac{\mathbf{B}}{2}; \kappa\right) E_{\text{in}}(\mathbf{x}_{\text{in}}, \boldsymbol{\alpha}; \kappa), \quad (5a)$$

$$E_{2,\text{ap}}(\mathbf{x}_{\text{in}}, \boldsymbol{\alpha}; \kappa) = A_2\left(\mathbf{x}_{\text{in}} + \frac{\mathbf{B}}{2}; \kappa\right) E_{\text{in}}(\mathbf{x}_{\text{in}}, \boldsymbol{\alpha}; \kappa), \quad (5b)$$

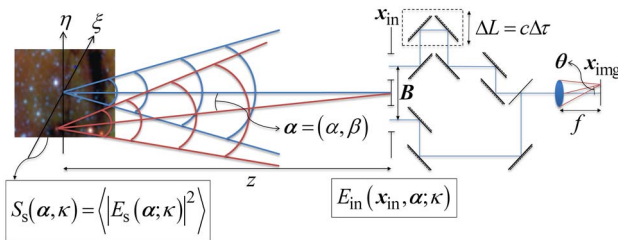


Fig. 1. Simplified diagram of a wide-field spatospectral interferometer for a fixed baseline, showing coordinate relationships and basic system configuration.

where $E_{1,\text{ap}}$ and $E_{2,\text{ap}}$ are implicitly functions of \mathbf{B} as well as t . In practice, the two light-collecting apertures A_1 and A_2 , which could be afocal telescopes, are likely to have some differences that would amount to different pupil aberrations, which may be wave-number dependent, and have possible amplitude variations across each. Such an aperture function can be defined, for example, as

$$A_n(\mathbf{x}_{\text{in}}; \kappa) = \begin{cases} a_n(\mathbf{x}_{n,\text{ap}}; \kappa) e^{i\Phi_n(\mathbf{x}_{n,\text{ap}}; \kappa)}, & |\mathbf{x}_{\text{in}}| \leq D/2 \\ 0, & |\mathbf{x}_{\text{in}}| > D/2 \end{cases} \quad (6)$$

where $\mathbf{x}_{n,\text{ap}}$ is the coordinate system centered on the n th aperture, a_n and Φ_n are the nonnegative amplitude and the phase across the n th aperture, respectively, and $|\cdot|$ denotes the Euclidean norm of a vector. This definition for the aperture function transmits the correct portion of the electric field for each baseline, while preventing a_n and Φ_n from having baseline dependence. Note that the support of a_n need not be circular as assumed in Eq. (6).

From the apertures, the field in one arm of the interferometer is time (path) delayed relative to the field in the other arm before the fields are combined at a beam splitter such that they are co-aligned and now share the same coordinate system. We denote the time delays induced by the two arms of the interferometer as τ_1 and τ_2 . The equivalent path delays are related through $L_n = c\tau_n$. Combining the fields at the interferometer is equivalent to shifting the fields in Eq. (5) such that A_1 and A_2 become collocated within the established coordinate system. For simplicity, we will assume that the coordinate system where the fields are combined is given by $\mathbf{x}_{\text{pup}} = \mathbf{x}_{\text{in}}$. We have chosen to relabel the coordinate system at which the fields are combined because it is possible to design a system where \mathbf{x}_{pup} is shifted relative to \mathbf{x}_{in} , which only affects the following analysis by changing the nominal values of τ_1 and τ_2 .

We combine this information with Eq. (5) in order to express the fields from arm 1 and arm 2 of the interferometer as

$$\begin{aligned} E_{1,\text{pup}}(\mathbf{x}_{\text{pup}}, \boldsymbol{\alpha}; \kappa) &= E_{1,\text{ap}}\left(\mathbf{x}_{\text{pup}} + \frac{\mathbf{B}}{2}, \boldsymbol{\alpha}; \kappa\right) \\ &= A_1(\mathbf{x}_{\text{pup}}; \kappa) E_{\text{in}}\left(\mathbf{x}_{\text{pup}} + \frac{\mathbf{B}}{2}, \boldsymbol{\alpha}; \kappa\right) \\ &= \gamma_1 e^{i\varphi_1(\kappa)} e^{i2\pi\kappa[z-c(t+\tau_1)]} \exp\left[i\pi \frac{\kappa}{z} \left(\mathbf{x}_{\text{pup}} + \frac{1}{2}\mathbf{B}\right)^2\right] E_s(\boldsymbol{\alpha}; \kappa) \\ &\quad \times A_1(\mathbf{x}_{\text{pup}}; \kappa) \exp(i\pi\kappa z \boldsymbol{\alpha}^2) \exp\left[i2\pi\kappa \boldsymbol{\alpha} \cdot \left(\mathbf{x}_{\text{pup}} + \frac{1}{2}\mathbf{B}\right)\right], \end{aligned} \quad (7a)$$

$$\begin{aligned} E_{2,\text{pup}}(\mathbf{x}_{\text{pup}}, \boldsymbol{\alpha}; \kappa) &= E_{2,\text{ap}}\left(\mathbf{x}_{\text{pup}} - \frac{\mathbf{B}}{2}, \boldsymbol{\alpha}; \kappa\right) \\ &= \gamma_1 e^{i\varphi_2(\kappa)} e^{i2\pi\kappa[z-c(t+\tau_2)]} \exp\left[i\pi \frac{\kappa}{z} \left(\mathbf{x}_{\text{pup}} - \frac{1}{2}\mathbf{B}\right)^2\right] E_s(\boldsymbol{\alpha}; \kappa) \\ &\quad \times A_2(\mathbf{x}_{\text{pup}}; \kappa) \exp(i\pi\kappa z \boldsymbol{\alpha}^2) \exp\left[i2\pi\kappa \boldsymbol{\alpha} \cdot \left(\mathbf{x}_{\text{pup}} - \frac{1}{2}\mathbf{B}\right)\right], \end{aligned} \quad (7b)$$

where $E_{1,\text{pup}}$ and $E_{2,\text{pup}}$ are implicitly functions of τ_1 and τ_2 , and $\varphi_1(\kappa)$ and $\varphi_2(\kappa)$ are the additional piston phases acquired during non-common path propagation from beam splitters and reflections off mirrors in the system. Assuming that $\varphi_1(\kappa)$ and $\varphi_2(\kappa)$ are independent of wavenumber and that mirror reflections in the arms of the interferometer are the only contributors to φ_1 and φ_2 , then $\Delta\varphi = \varphi_2 - \varphi_1 = m\pi$ for some integer m , depending on the number of reflections. Note that for a non-ideal system, one must pay more attention to the transmission and reflection coefficients of all optical elements in the interferometer, especially for all elements before the beam splitter.

The above fields are then combined at the beam splitter, often considered the exit pupil of the interferometer, generating new fields, E_3 and E_4 , at the two output ports of the splitter:

$$E_3 = r_{\text{bs}}E_1 + t_{\text{bs}}E_2, \quad (8a)$$

$$E_4 = t_{\text{bs}}E_1 + r_{\text{bs}}E_2, \quad (8b)$$

where r_{bs} and t_{bs} are the beam splitter's amplitude reflection coefficient and amplitude transmission coefficient, respectively. The above equations are valid in both the pupil and image planes, so we will be more explicit about input variables when E_3 and E_4 are computed later. For a lossless, symmetric beam splitter, the phase difference between r_{bs} and t_{bs} is $\pi/2$ [7]. Also, assume a 50/50 beam splitter such that $|r_{\text{bs}}| = |t_{\text{bs}}| = 1/\sqrt{2}$. The intensity reflection and transmission coefficients are then $R = |r_{\text{bs}}|^2 = 1/2$ and $T = |t_{\text{bs}}|^2 = 1/2$. The wide-field extension of double-Fourier interferometry can be obtained by adding an imaging lens after the beam combiner such that if either one of the beams is blocked before beam combination, a panchromatic image of the source is obtained at the detector array. Appendix A discusses connections to coherence theory, which are best formulated just after beam combination. For the time being, the most important result, as shown in Appendix A, is that the source is assumed to be spatially and spectrally incoherent, resulting in the following relationships [Eqs. (A8) and (A9)]:

$$\langle E_s^*(\alpha; \kappa) E_s(\alpha'; \kappa') \rangle = W_s(\alpha, \alpha'; \kappa) \delta(\kappa - \kappa') \\ \propto \sigma S_s(\alpha; \kappa) \delta(\alpha - \alpha', \kappa - \kappa'), \quad (9)$$

$$\langle |E_s(\alpha; \kappa)|^2 \rangle \propto \sigma S_s(\alpha; \kappa), \quad (10)$$

where W_s and S_s are the cross-spectral density and spectral density, respectively, of the source; $\sigma = \lambda^2/\pi = (\pi\kappa^2)^{-1}$ is the proportionality constant when the source is incoherent (Lambertian) ([8] Eqs. 5.5–19); and $\langle \cdot \rangle$ is the ensemble average, equivalent to the time average from start time t_a to end time t_b defined by

$$\langle \dots \rangle = \frac{1}{t_b - t_a} \int_{t_a}^{t_b} \dots dt. \quad (11)$$

Although there are proportionalities in Eqs. (9) and (10), we will take them to be equalities because the scaling factors affect the overall scaling of the spectral density rather than its shape. The delta function in Eq. (9) helps to reduce the dimensionality of the integrals related to the interference of the two beams in the following section.

B. Wide-Field Image Formation

Instead of propagating the fields E_3 and E_4 [Eq. (8)] just after the beam splitter to the image plane, it may be easier to consider propagating E_1 and E_2 [Eq. (7)] to the image plane individually and then generate fields E_3 and E_4 at the image plane using Eq. (8). The image plane coordinates, \mathbf{x}_{img} , have the same transverse origin (optical axis) as the pupil coordinates, \mathbf{x}_{pup} , and are defined as

$$\boldsymbol{\theta} = (\theta_x, \theta_y) = \frac{(x_{\text{img}}, y_{\text{img}})}{f} = \frac{\mathbf{x}_{\text{img}}}{f}, \quad (12)$$

where f is the effective focal length of the imaging lens subsequent to beam combination. Any phases acquired after beam combination are common path, will cancel when the intensity of the combined field is taken in the measurement plane, and will not contribute to the interferogram. For this reason, we will ignore the quadratic phase term that depends on image plane location and constant-phase terms in the following propagations. From Eq. (7),

$$E_{1,\text{im}}(\boldsymbol{\theta}, \boldsymbol{\alpha}; \kappa) \\ = \frac{\kappa}{if} \int E_{1,\text{pup}}(\mathbf{x}_{\text{pup}}, \boldsymbol{\alpha}; \kappa) e^{-i2\pi\kappa\boldsymbol{\theta} \cdot \mathbf{x}_{\text{pup}}} d^2\mathbf{x}_{\text{pup}} \\ = \gamma_2 e^{i\varphi_1(\kappa)} \exp\left(i\pi \frac{\kappa}{4z} \mathbf{B}^2\right) e^{i2\pi\kappa[z - c(\tau + \tau_1)]} E_s(\boldsymbol{\alpha}; \kappa) \\ \times \exp(i\pi\kappa z \boldsymbol{\alpha}^2) e^{i\pi\kappa\boldsymbol{\alpha} \cdot \mathbf{B}} \int A_1(\mathbf{x}_{\text{pup}}; \kappa) \exp\left(i\pi \frac{\kappa}{z} \mathbf{x}_{\text{pup}}^2\right) \\ \times \exp\left[-i2\pi\kappa \left(\boldsymbol{\theta} - \boldsymbol{\alpha} - \frac{\mathbf{B}}{2z}\right) \cdot \mathbf{x}_{\text{pup}}\right] d^2\mathbf{x}_{\text{pup}} \\ = \gamma_2 e^{i\varphi_1(\kappa)} \exp\left(i\pi \frac{\kappa}{4z} \mathbf{B}^2\right) e^{i2\pi\kappa[z - c(\tau + \tau_1)]} \exp(i\pi\kappa z \boldsymbol{\alpha}^2), \\ \times b_1 \left[\left(\boldsymbol{\theta} - \frac{\mathbf{B}}{2z}\right) - \boldsymbol{\alpha}; \kappa \right] E_s(\boldsymbol{\alpha}; \kappa) e^{i\pi\kappa\boldsymbol{\alpha} \cdot \mathbf{B}}, \quad (13a)$$

$$E_{2,\text{im}}(\boldsymbol{\theta}, \boldsymbol{\alpha}; \kappa) \\ = \frac{\kappa}{if} \int E_{2,\text{pup}}(\mathbf{x}_{\text{pup}}, \boldsymbol{\alpha}; \kappa) e^{-i2\pi\kappa\boldsymbol{\theta} \cdot \mathbf{x}_{\text{pup}}} d^2\mathbf{x}_{\text{pup}} \\ = \gamma_2 e^{i\varphi_2(\kappa)} \exp\left(i\pi \frac{\kappa}{4z} \mathbf{B}^2\right) e^{i2\pi\kappa[z - c(\tau + \tau_2)]} \exp(i\pi\kappa z \boldsymbol{\alpha}^2) \\ \times b_2 \left[\left(\boldsymbol{\theta} + \frac{\mathbf{B}}{2z}\right) - \boldsymbol{\alpha}; \kappa \right] E_s(\boldsymbol{\alpha}; \kappa) e^{-i\pi\kappa\boldsymbol{\alpha} \cdot \mathbf{B}}, \quad (13b)$$

where

$$b_n(\boldsymbol{\theta}; \kappa) = \int A_n(\mathbf{x}_{\text{pup}}; \kappa) \exp\left(i\pi \frac{\kappa}{z} \mathbf{x}_{\text{pup}}^2\right) \\ \times \exp(-i2\pi\kappa\boldsymbol{\theta} \cdot \mathbf{x}_{\text{pup}}) d^2\mathbf{x}_{\text{pup}} \quad (14)$$

is the coherent impulse response, or amplitude spread function, for the n th aperture, and

$$\gamma_2 = \gamma_1 \frac{\kappa}{if} = \frac{iz}{\kappa} \frac{\kappa}{if} = \frac{z}{f}. \quad (15)$$

Note that $\int \dots d^2\mathbf{x}_{\text{pup}}$ is understood to be a 2D integral. We reserve integration over source angle and wavenumber for when we compute the image intensity; for simplicity, we also assume

unit magnification between α and θ . Notice that if the baseline length is not small compared with the source distance, the image location will be a function of the baseline, where the fields from each arm shift in opposing directions. We can ignore this feature for astronomical imaging, but this effect must be considered for laboratory experiments if the source to be measured by the interferometer is not aligned properly to the front focal plane of the collimating optic, which is needed to simulate a distant source. It is also worth noting that we can ignore the quadratic phase term in Eq. (14) if we carefully position the detector to be at the best focus for any given image measurement, but the quadratic phase is negligible for astronomical sources and for laboratory sources that are properly collimated.

The total intensity at the image plane is found by taking the squared magnitude of E_3 or E_4 and then taking the time average using Eq. (11). The total field at the image plane depends on contributions from all wavelengths and field angles (although each location in the image plane is associated with a narrow range of angles). In the rest of the derivation, we will use the assumption that the sources are spatially and spectrally incoherent, as summarized mathematically by Eqs. (9) and (10). If we block either arm of the interferometer, we are left with the image intensity contributions from each arm independently. Using Eqs. (9)–(11) and (13),

$$\begin{aligned}
 I_1(\theta) &= \left\langle \left| \int_0^\infty \int_{-1}^1 E_{1,\text{im}}(\theta, \alpha; \kappa) d^2\alpha d\kappa \right|^2 \right\rangle \\
 &= |\gamma_2|^2 \int_0^\infty \int_0^\infty \int_{-1}^1 \int_{-1}^1 h_1^* \left[\left(\theta - \frac{\mathbf{B}}{2z} \right) - \alpha; \kappa \right] \\
 &\quad \times h_1 \left[\left(\theta - \frac{\mathbf{B}}{2z} \right) - \alpha'; \kappa' \right] \langle E_s^*(\alpha; \kappa) E_s(\alpha'; \kappa') \rangle \\
 &\quad \times d^2\alpha' d^2\alpha d\kappa' d\kappa \\
 &= |\gamma_3|^2 \int_0^\infty \int_{-1}^1 p_{1,1} \left[\left(\theta - \frac{\mathbf{B}}{2z} \right) - \alpha; \kappa \right] S_s(\alpha; \kappa) d^2\alpha d\kappa,
 \end{aligned} \tag{16a}$$

$$\begin{aligned}
 I_2(\theta) &= \left\langle \left| \int_0^\infty \int_{-1}^1 E_{2,\text{im}}(\theta, \alpha; \kappa) d^2\alpha d\kappa \right|^2 \right\rangle \\
 &= |\gamma_3|^2 \int_0^\infty \int_{-1}^1 p_{2,2} \left[\left(\theta + \frac{\mathbf{B}}{2z} \right) - \alpha; \kappa \right] \\
 &\quad \times S_s(\alpha; \kappa) d^2\alpha d\kappa,
 \end{aligned} \tag{16b}$$

$$\gamma_3 = \sigma^{1/2} \gamma_2 \frac{\kappa}{if} = \frac{1}{\pi^{1/2} \kappa f} \frac{z}{if} = \frac{z}{i\pi^{1/2} f^2}, \tag{17}$$

where the point spread function (PSF) for the n th arm of the interferometer is given by

$$p_{n,n}(\theta, \kappa) = |h_n(\theta, \kappa)|^2. \tag{18}$$

Using Eqs. (8), (9), (11), (13), (16), and (17), the image intensities for the combined fields for a fixed delay difference $\Delta\tau = \tau_2 - \tau_1$ are then

$$\begin{aligned}
 I_3(\theta) &= \left\langle \left| \int_0^\infty \int_{-1}^1 E_{3,\text{im}}(\theta, \alpha; \kappa) d^2\alpha d\kappa \right|^2 \right\rangle \\
 &= \left\langle \left| \int_0^\infty \int_{-1}^1 [r_{\text{bs}} E_{1,\text{im}}(\theta, \alpha; \kappa) + t_{\text{bs}} E_{2,\text{im}}(\theta, \alpha; \kappa)] d^2\alpha d\kappa \right|^2 \right\rangle \\
 &= RI_1(\theta) + TI_2(\theta) \\
 &\quad + 2\text{Re} \left[r_{\text{bs}}^* t_{\text{bs}} \int_0^\infty \int_0^\infty \int_{-1}^1 \int_{-1}^1 \langle E_{1,\text{im}}^*(\theta, \alpha; \kappa) \right. \\
 &\quad \left. \times E_{2,\text{im}}(\theta, \alpha'; \kappa') \rangle d^2\alpha' d^2\alpha d\kappa' d\kappa \right] \\
 &= \frac{1}{2} [I_1(\theta) + I_2(\theta)] \\
 &\quad + \text{Re} \left[e^{i\frac{\pi}{2}} \int_0^\infty \int_0^\infty W_{12}^{\text{im}}(\theta; \kappa') \delta(\kappa - \kappa') d\kappa' d\kappa \right] \\
 &= \frac{1}{2} [I_1(\theta) + I_2(\theta)] - \text{Im} \left[\int_0^\infty W_{12}^{\text{im}}(\theta; \kappa) d\kappa \right],
 \end{aligned} \tag{19a}$$

$$\begin{aligned}
 I_4(\theta) &= \left\langle \left| \int_0^\infty \int_{-1}^1 E_{4,\text{im}}(\theta, \alpha; \kappa) d^2\alpha d\kappa \right|^2 \right\rangle \\
 &= \frac{1}{2} [I_1(\theta) + I_2(\theta)] + \text{Im} \left[\int_0^\infty W_{12}^{\text{im}}(\theta; \kappa) d\kappa \right],
 \end{aligned} \tag{19b}$$

where

$$\begin{aligned}
 W_{12}^{\text{im}}(\theta; \kappa) &= \int_{-1}^1 \int_{-1}^1 \langle E_{1,\text{im}}^*(\theta, \alpha; \kappa) E_{2,\text{im}}(\theta, \alpha'; \kappa) \rangle d^2\alpha' d^2\alpha \\
 &= |\gamma_2|^2 \int_{-1}^1 \int_{-1}^1 e^{i\Delta\varphi(\kappa)} \exp \left(-i\pi \frac{\kappa}{4z} \mathbf{B}^2 \right) e^{-i\pi\kappa z \alpha^2} e^{-i2\pi\kappa[z-c(t+\tau_1)]} \\
 &\quad \times e^{-i\pi\kappa\alpha \cdot \mathbf{B}} \exp \left(i\pi \frac{\kappa}{4z} \mathbf{B}^2 \right) e^{i\pi\kappa z \alpha'^2} e^{i2\pi\kappa[z-c(t+\tau_2)]} e^{-i\pi\kappa\alpha' \cdot \mathbf{B}} \\
 &\quad \times h_1^* \left[\left(\theta - \frac{\mathbf{B}}{2z} \right) - \alpha; \kappa \right] h_2 \left[\left(\theta + \frac{\mathbf{B}}{2z} \right) - \alpha'; \kappa \right] \\
 &\quad \times \langle E_s^*(\alpha; \kappa) E_s(\alpha'; \kappa) \rangle d^2\alpha' d^2\alpha \\
 &= |\gamma_3|^2 e^{i\Delta\varphi(\kappa)} e^{-i2\pi\kappa c \Delta\tau} \\
 &\quad \times \int_{-1}^1 h_1^* \left[\left(\theta - \frac{\mathbf{B}}{2z} \right) - \alpha; \kappa \right] h_2 \left[\left(\theta + \frac{\mathbf{B}}{2z} \right) - \alpha; \kappa \right] \\
 &\quad \times e^{-i2\pi\kappa\alpha \cdot \mathbf{B}} S_s(\alpha; \kappa) d^2\alpha
 \end{aligned} \tag{20}$$

is the cross-spectral density between the fields from the interferometer's entrance apertures after propagation to the interferometer's image plane. In the above equations, we applied the assumptions that $R = T = 1/2$ and that the phase difference between r_{bs} and t_{bs} is $\pi/2$. We also assume that the field is stationary in the wide sense so that the interference terms, $\langle E_{1,\text{im}}^* E_{2,\text{im}} \rangle$ and W_{12}^{im} , do not vary with start time t_a in Eq. (11), but is implicitly a function of $\Delta\tau$, and that $S_s(\alpha; \kappa)$ does not vary over the course of data collection. This technique is not well suited for imaging quickly changing sources. Equations (19a) and (19b) can be combined into a single equation for the image intensity:

$$I_{3,4}(\boldsymbol{\theta}) = \frac{1}{2}[I_1(\boldsymbol{\theta}) + I_2(\boldsymbol{\theta})] \mp \text{Im} \left[\int_0^\infty W_{12}^{\text{im}}(\boldsymbol{\theta}; \kappa) d\kappa \right]. \quad (21)$$

The coherent impulse responses due to the apertures are now addressed. Equation (13) shows that, in general, the locations of the amplitude spread functions depend on the ratio of the baseline separation to the source distance. For astronomical sources, the source distance is much greater than the baseline length, allowing the baseline dependence to be dropped if the image shift is negligible compared with the interferometer's finest resolution [see Eq. (32)]:

$$\frac{|\mathbf{B}|_{\text{max}}}{2z} \frac{1}{(\kappa_{\text{max}} |\mathbf{B}|_{\text{max}})^{-1}} \ll 1, \\ z \gg \frac{1}{2} \kappa_{\text{max}} |\mathbf{B}|_{\text{max}}^2, \quad (22)$$

where κ_{max} is largest measured wavenumber and $|\mathbf{B}|_{\text{max}}$ is the longest baseline length. For experimental setups that must simulate distant sources using an image at the focus of a collimating mirror, a steering mirror can be used to ensure that the coherent impulse responses overlap for all baseline lengths. For these reasons, the baseline dependence on image location will be ignored for the rest of this paper, and Eqs. (16) and (20) become

$$I_1(\boldsymbol{\theta}) = |\gamma_3|^2 \int_0^\infty \int_{-1}^1 p_{1,1}(\boldsymbol{\theta} - \boldsymbol{\alpha}; \kappa) S_s(\boldsymbol{\alpha}; \kappa) d^2\boldsymbol{\alpha} d\kappa, \quad (23a)$$

$$I_2(\boldsymbol{\theta}) = |\gamma_3|^2 \int_0^\infty \int_{-1}^1 p_{2,2}(\boldsymbol{\theta} - \boldsymbol{\alpha}; \kappa) S_s(\boldsymbol{\alpha}; \kappa) d^2\boldsymbol{\alpha} d\kappa, \quad (23b)$$

$$W_{12}^{\text{im}}(\boldsymbol{\theta}; \kappa) = |\gamma_3|^2 e^{i\Delta\varphi(\kappa)} e^{-i2\pi\kappa\Delta L} \\ \times \int_{-1}^1 p_{1,2}(\boldsymbol{\theta} - \boldsymbol{\alpha}; \kappa) e^{-i2\pi\kappa\boldsymbol{\alpha}\cdot\mathbf{B}} S_s(\boldsymbol{\alpha}; \kappa) d^2\boldsymbol{\alpha}, \quad (24)$$

where the optical delay has been converted to units of length using $\Delta L = c\Delta\tau$ and where the spectral point spread functions (SPSFs) [4,5] of the apertures are defined as

$$p_{m,n}(\boldsymbol{\theta}; \kappa) = h_m^*(\boldsymbol{\theta}; \kappa) h_n(\boldsymbol{\theta}; \kappa), \quad (25)$$

where m and n are the indices of the apertures in the interferometer. Inserting Eq. (24), Eq. (21) becomes

$$I_{3,4}(\boldsymbol{\theta}) = \frac{1}{2}[I_1(\boldsymbol{\theta}) + I_2(\boldsymbol{\theta})] \mp |\gamma_3|^2 \int_0^\infty \int_{-1}^1 S_s(\boldsymbol{\alpha}; \kappa) \\ \times \text{Im} [e^{i\Delta\varphi(\kappa)} p_{1,2}(\boldsymbol{\theta} - \boldsymbol{\alpha}; \kappa) e^{-i2\pi\kappa(\boldsymbol{\alpha}\cdot\mathbf{B} + \Delta L)}] d^2\boldsymbol{\alpha} d\kappa. \quad (26)$$

Analogous to how the van Cittert–Zernike theorem is applicable to source distances that are shorter than allowed by the Fraunhofer approximation, Eq. (26) was derived using the more general Fresnel propagations, yet most of the quadratic phase terms have vanished. Only the quadratic phase term of Eq. (14) remains, but its impact is negligible for astronomical sources, especially when Eq. (22) holds, and can be mitigated in the lab by placing the detector at the best focus of the imaging system.

Equation (26) represents a complicated Fourier relationship. Because the order of integration over source angle and wavenumber can be interchanged for an incoherent source, we will consider integration over source angle first; with this assumption, (i) $\boldsymbol{\alpha}$ and $\kappa\mathbf{B}$, and (ii) κ and ΔL (or ν and $\Delta\tau$) are revealed to be Fourier conjugate variables. In fact, the name

double-Fourier interferometry [9] comes from the idea that we have two Fourier transform relationships, one spatial and one spectral, contributing to each measurement.

To simplify Eq. (26) even further, temporarily assume that both of the interferometer's collecting apertures are perfectly symmetric and identical, in which case

$$p_{1,1}(\boldsymbol{\theta}; \kappa) = p_{2,2}(\boldsymbol{\theta}; \kappa) = p_{1,2}(\boldsymbol{\theta}; \kappa), \quad (27)$$

$$I_1(\boldsymbol{\theta}) = I_2(\boldsymbol{\theta}), \quad (28)$$

and

$$I_{3,4}(\boldsymbol{\theta}) = I_1(\boldsymbol{\theta}) \mp |\gamma_3|^2 \int_0^\infty \int_{-1}^1 p_{1,1}(\boldsymbol{\theta} - \boldsymbol{\alpha}; \kappa) S_s(\boldsymbol{\alpha}; \kappa) \\ \times \text{Im} [e^{i\Delta\varphi(\kappa)} e^{-i2\pi\kappa(\boldsymbol{\alpha}\cdot\mathbf{B} + \Delta L)}] d^2\boldsymbol{\alpha} d\kappa \\ = I_1(\boldsymbol{\theta}) \pm |\gamma_3|^2 \int_0^\infty \int_{-1}^1 p_{1,1}(\boldsymbol{\theta} - \boldsymbol{\alpha}; \kappa) S_s(\boldsymbol{\alpha}; \kappa) \\ \times \sin[2\pi\kappa(\boldsymbol{\alpha}\cdot\mathbf{B} + \Delta L) - \Delta\varphi(\kappa)] d^2\boldsymbol{\alpha} d\kappa. \quad (29)$$

Due to the assumption of perfect symmetry, the phase of $p_{1,2}$ above has vanished. In practice, instrumental phases including the phase of $p_{1,2}$ and $\Delta\varphi(\kappa)$ can be calibrated if they are known. This simplified model of the measured intensity shows that, if we take image measurements for many different delay values at a single baseline, a fringe packet as a function of ΔL exists for every image location $\boldsymbol{\theta}$. The position of the fringe is dependent on both the source location and baseline, while the width and shape of the fringe packet depend on both the source spectral density at the corresponding source location and $\Delta\varphi(\kappa)$. A simplified measurement model similar to the form shown in Eq. (29) has been used to demonstrate how a high-resolution hyperspectral image can be reconstructed from a set of these interferometric measurements {[1], Eq. (12); [2], Eq. (4)}; however, we will start our derivation of the “dirty” (i.e., direct Fourier inversion) high-resolution hyperspectral image directly from the more general Eq. (26).

3. MEASUREMENT SET AND SAMPLING

Before getting into the details of reconstructing a high-resolution hyperspectral image, it is instructive to discuss the set of interferometric measurements that are used to generate the high-resolution image. Given a fixed baseline and delay length, the interferometer captures a 2D panchromatic image of the astronomical source having the resolution of the individual apertures (assumed to be same size). We assume the sampling of the detector is matched to the resolution of a single aperture so that the Nyquist sampling criteria is satisfied. It also might be possible to sub-Nyquist sample the images and obtain super-resolved images relative to the pixel pitch through a post-processing dealiasing technique developed for Fizeau Fourier transform imaging spectroscopy (FTIS) [10]; however, we will continue to assume that all measured intensities are Nyquist sampled according to the diameters of the input apertures. For the sake of simplicity, all measurements will be assumed to be completely discrete in the sense that all parts of the interferometer are stationary for each measurement with fixed baseline and delay values. Keeping the baseline fixed, a set of measurements is taken for various delay lengths resulting

in one measurement cube, where two dimensions are the spatial dimensions of the array detector and the third dimension is delay length, ΔL , which can be monitored using laser metrology [11]. Due to the Fourier relationship between ΔL and wavenumber, κ , sampling theory can be used to determine the desired scan range and sampling of the delay line to match the desired spectral resolution and range of the final reconstructed image:

$$\text{resolution: } \Delta\kappa_{\min} \approx \frac{1}{\Delta L_{\max} - \Delta L_{\min}} = \frac{1}{2\Delta L_{\max}}, \quad (30)$$

$$\text{range: } \kappa_{\max} \approx \frac{N_L}{2} \Delta\kappa_{\min} = \frac{N_L}{4\Delta L_{\max}}, \quad (31)$$

where N_L is the number of Nyquist-sampled delay-line samples from $-\Delta L_{\max}$ to ΔL_{\max} . The position of the fringe packet is linearly related to image location; thus, in order to measure the fringe for all field points, the delay line length is assumed to extend equally in both directions about the zero delay position, meaning $\Delta L_{\min} = -\Delta L_{\max}$. We will return to this idea shortly in order to discuss the interferometer's field-of-view (FOV). Conversely, the range of recovered wavenumbers is κ_{\max} because only positive values of κ are physical. In fact, due to system transmissivity and detector limitations, the interferometer's bandpass is less than κ_{\max} , suggesting $0 < \kappa_{\min} < \kappa_{\max}$; knowledge of the bandpass can be exploited, provided the measurements have an adequate signal-to-noise ratio, thus allowing the delay line sampling to be relaxed as for FTIS [12].

The angular resolution of a sparse-aperture interferometer is related to the inverse of the largest spatial frequency probed by the imaging interferometer, $\kappa_{\max}|\mathbf{B}|_{\max}$. Using this idea, the resolution of an imaging interferometer is

$$\Delta\alpha_{\min} = (\kappa_{\max}|\mathbf{B}|_{\max})^{-1} = \frac{\lambda_{\min}}{|\mathbf{B}|_{\max}}. \quad (32)$$

Although this equation defines the best possible angular (spatial) resolution of the interferometer, the overall quality of the reconstructed image at this resolution also is related to baseline sampling as well as the signal-to-noise ratio of each measurement. We will briefly return to the idea of baseline sampling in Section 4.D. It should be noted that images captured at different baseline orientations are rotated according to the baseline orientation because we assume that, by design, the entire interferometer, including all optical elements from the input apertures to the detectors, is rotating about its line-of-sight while the source orientation stays fixed (or equivalently that the source is rotating while the interferometer orientation stays fixed), and this rotation must be accounted for.

The full FOV of a double-Fourier interferometer could be limited by various aspects of the system, depending on overall system design, including the full FOV of each individual aperture, the size of steering mirrors in both arms of interferometer, the number of samples across the array detector, and the length of the delay line. The dependency on ΔL_{\max} is due to the fact that, in order to accurately reconstruct the spectra of off-axis sources, the center of the fringe, whose position depends on source location and baseline length, must be measured.

Specifically, the argument of the sinusoid in Eq. (29) includes the term $(\boldsymbol{\alpha} \cdot \mathbf{B} + \Delta L)$, from which the zero path difference (ZPD), defined as the center of the fringe packet, is determined to be

$$\Delta L_{\text{ZPD}} = -\boldsymbol{\alpha} \cdot \mathbf{B}. \quad (33)$$

If we assume $\Delta\varphi(\kappa)$ is independent of κ in Eq. (29), then the envelope of the fringe packet is symmetric about ΔL_{ZPD} , where the envelope is maximal. If we keep the assumption that the fringe packets are symmetric, and assume that ΔL_{\max} and $|\mathbf{B}|_{\max}$ are fixed, then the FOV is limited by

$$\text{FOV} = |\boldsymbol{\alpha}|_{\max} - |\boldsymbol{\alpha}|_{\min} \approx \frac{-\Delta L_{\min}}{|\mathbf{B}|_{\max}} + \frac{\Delta L_{\max}}{|\mathbf{B}|_{\max}} = \frac{2\Delta L_{\max}}{|\mathbf{B}|_{\max}}. \quad (34)$$

If $\Delta\varphi(\kappa)$ is arbitrary, the fringe envelope is not necessarily symmetric, so it is important that ΔL_{\max} is large enough to measure out to $\pm|\Delta L_{\text{ZPD}}|_{\max} = \pm|\boldsymbol{\alpha} \cdot \mathbf{B}|_{\max}$ at the least. In this sense, Eq. (34) is a slightly overstated estimate for the full FOV of an arbitrary wide-field double-Fourier interferometer when ΔL_{\max} and $|\mathbf{B}|_{\max}$ are fixed.

4. DIRECT HYPERSPECTRAL IMAGE SYNTHESIS

A. Preprocessing of Data

Now that the interferometric measurement set and spatial/spectral resolution limits have been discussed, the algorithm to reconstruct a high-resolution hyperspectral image can be introduced. Let us assume that we have already preregistered all images in the measurement set using a method akin to phase referencing in optical stellar interferometry ([13], 2.2.2), which has been introduced for double-Fourier interferometry by Mariotti and Ridgway [9]. The image reconstruction approach provided herein is based on processing the entire FOV at once, as opposed to existing algorithms that have been demonstrated on a pixel-by-pixel basis [14]. The first few steps involved in reconstructing the "dirty" image cube are similar to reconstructing spectra in Fourier transform spectroscopy measurements. Reconsider the result from Eq. (26) to be a 5D measurement set where two dimensions correspond to image location $\boldsymbol{\theta}$, two dimensions correspond to the baseline vector \mathbf{B} , and one dimension to the delay ΔL between arms of the interferometer. Including \mathbf{B} and ΔL explicitly in the list of arguments, we have

$$I_{3,4}(\boldsymbol{\theta}, \mathbf{B}; \Delta L) = I_{\text{bias}}(\boldsymbol{\theta}) \mp |\gamma_3|^2 \int_0^\infty \int_{-1}^1 S_s(\boldsymbol{\alpha}; \kappa) \times \text{Im} \left[e^{i\Delta\varphi(\kappa)} p_{1,2}(\boldsymbol{\theta} - \boldsymbol{\alpha}; \kappa) e^{-i2\pi\kappa(\boldsymbol{\alpha} \cdot \mathbf{B} + \Delta L)} \right] d^2\boldsymbol{\alpha} d\kappa, \quad (35)$$

where we define

$$I_{\text{bias}}(\boldsymbol{\theta}) = \frac{1}{2}[I_1(\boldsymbol{\theta}) + I_2(\boldsymbol{\theta})] \approx \lim_{\Delta L_{\max} \rightarrow \infty} \frac{1}{2\Delta L_{\max}} \int_{-\Delta L_{\max}}^{\Delta L_{\max}} I_{3,4}(\boldsymbol{\theta}, \mathbf{B}; \Delta L) d\Delta L, \quad (36)$$

which is independent of ΔL and \mathbf{B} . The limit in Eq. (36) applied to the interference term in Eq. (35) approaches a value of zero because the interference term is essentially the sum of many sinusoids of varying amplitude and frequency, and the integral of each sinusoid approaches zero when $\Delta L_{\max} \rightarrow \infty$. The validity of the approximation in Eq. (36), which allows the estimation of $I_{\text{bias}}(\boldsymbol{\theta})$ directly from the datacube for each baseline, depends on the delay line range and sampling because we want the fluctuations in the interference term to approach a value of zero when averaging over all delay line positions for a single baseline.

Assuming that measurements at all baselines have been rotated and registered to one orientation, a bias-subtracted interferogram can be generated by subtracting off the fringe bias at each pixel:

$$\begin{aligned} I_{\text{bs}}^r(\boldsymbol{\theta}, \mathbf{B}; \Delta L) &= I_{3,4}(\boldsymbol{\theta}, \mathbf{B}; \Delta L) - I_{\text{bias}}(\boldsymbol{\theta}) \\ &= \mp |\gamma_3|^2 \int_0^\infty \int_{-1}^1 S_s(\boldsymbol{\alpha}; \kappa) \\ &\quad \times \text{Im}[e^{i\Delta\varphi(\kappa)} p_{1,2}(\boldsymbol{\theta} - \boldsymbol{\alpha}; \kappa) e^{-i2\pi\kappa(\boldsymbol{\alpha}\cdot\mathbf{B} + \Delta L)}] d^2\boldsymbol{\alpha} d\kappa. \end{aligned} \quad (37)$$

The r superscript is meant to convey that the above array consists of strictly real values.

B. Spectral Processing

Although I_{bs}^r is real valued, it is derived from an underlying analytic signal describing the spectral distribution of the source, where only positive wavenumbers are physical. This suggests that the imaginary values associated with the analytic signal can be determined from the real values through a Hilbert transform over the delay line variable, ΔL :

$$\begin{aligned} I_{\text{bs}}^i(\boldsymbol{\theta}, \mathbf{B}; \Delta L) &= H[I_{\text{bs}}^r(\boldsymbol{\theta}, \mathbf{B}; \Delta L)] \\ &= \pm |\gamma_3|^2 \int_0^\infty \int_{-1}^1 S_s(\boldsymbol{\alpha}; \kappa) \\ &\quad \times \text{Re}[e^{i\Delta\varphi(\kappa)} p_{1,2}(\boldsymbol{\theta} - \boldsymbol{\alpha}; \kappa) e^{-i2\pi\kappa(\boldsymbol{\alpha}\cdot\mathbf{B} + \Delta L)}] d^2\boldsymbol{\alpha} d\kappa, \end{aligned} \quad (38)$$

and we can define the complex analytic signal by

$$\begin{aligned} I_{\text{bs}}(\boldsymbol{\theta}, \mathbf{B}; \Delta L) &= I_{\text{bs}}^r(\boldsymbol{\theta}, \mathbf{B}; \Delta L) + i I_{\text{bs}}^i(\boldsymbol{\theta}, \mathbf{B}; \Delta L) \\ &= \pm i |\gamma_3|^2 \int_0^\infty \int_{-1}^1 p_{1,2}(\boldsymbol{\theta} - \boldsymbol{\alpha}; \kappa) S_s(\boldsymbol{\alpha}; \kappa) \\ &\quad \times \exp[i\Delta\varphi(\kappa) - i2\pi\kappa(\boldsymbol{\alpha}\cdot\mathbf{B} + \Delta L)] d^2\boldsymbol{\alpha} d\kappa. \end{aligned} \quad (39)$$

Notice that, when the analytic signal is generated from the measured interferogram, the result looks like the same Fourier transform relationship as in Eq. (26). Consequently, the spectrum of each spatial sample in the image of the source for a given baseline can be recovered by taking the inverse Fourier transform of I_{bs} over ΔL :

$$\begin{aligned} S_i(\boldsymbol{\theta}, \mathbf{B}; \kappa) &= \int_{-\Delta L_{\max}}^{\Delta L_{\max}} I_{\text{bs}}(\boldsymbol{\theta}, \mathbf{B}; \Delta L) e^{i2\pi\kappa\Delta L} d\Delta L \\ &= \pm i |\gamma_3|^2 \int_0^\infty \left(\int_{-\Delta L_{\max}}^{\Delta L_{\max}} e^{-i2\pi\kappa'\Delta L} e^{i2\pi\kappa\Delta L} d\Delta L \right) \int_{-1}^1 p_{1,2}(\boldsymbol{\theta} - \boldsymbol{\alpha}; \kappa') \\ &\quad \times S_s(\boldsymbol{\alpha}; \kappa') \exp[i\Delta\varphi(\kappa) - i2\pi\kappa(\boldsymbol{\alpha}\cdot\mathbf{B} + \Delta L)] d^2\boldsymbol{\alpha} d\kappa \\ &= \pm i |\gamma_3|^2 \int_0^\infty 2\Delta L_{\max} \text{sinc}[2\Delta L_{\max}(\kappa - \kappa')] \int_{-1}^1 p_{1,2}(\boldsymbol{\theta} - \boldsymbol{\alpha}; \kappa') \\ &\quad \times S_s(\boldsymbol{\alpha}; \kappa') e^{i\Delta\varphi(\kappa')} \exp(-i2\pi\kappa'\boldsymbol{\alpha}\cdot\mathbf{B}) d^2\boldsymbol{\alpha} d\kappa' \\ &= \pm i 2\Delta L_{\max} |\gamma_3|^2 \text{sinc}(2\Delta L_{\max}\kappa) \left[\int_{-1}^1 p_{1,2}(\boldsymbol{\theta} - \boldsymbol{\alpha}; \kappa) \right. \\ &\quad \left. \times S_s(\boldsymbol{\alpha}; \kappa) e^{i\Delta\varphi(\kappa)} \exp(-i2\pi\kappa\boldsymbol{\alpha}\cdot\mathbf{B}) d^2\boldsymbol{\alpha} \right] \\ &= \pm i 2\Delta L_{\max} |\gamma_3|^2 \text{sinc}(2\Delta L_{\max}\kappa) \\ &\quad \times \{ [S_s(\boldsymbol{\theta}; \kappa) \exp(-i2\pi\kappa\boldsymbol{\theta}\cdot\mathbf{B})] \overset{\kappa}{*} p_{1,2}(\boldsymbol{\theta}; \kappa) e^{i\Delta\varphi(\kappa)} \}, \end{aligned} \quad (40)$$

where the in-line asterisk $\overset{\kappa}{*}$ denotes a convolution in the κ dimension and $\overset{\theta}{*}$ represents a 2D convolution over the dimensions of $\boldsymbol{\theta}$. The above result is now an array of low-spatial-resolution, spatially spectrally filtered hyperspectral images, where the resolution in the spectral domain is limited by the sinc function of width $(2\Delta L_{\max})^{-1}$, and the spatial resolution is limited by the width of $p_{1,2}$, which is approximately $(\kappa D)^{-1}$ for individual pupils contained within a circle of diameter D . Although at this point in the image processing, Eq. (40) is a low-spatial-resolution hyperspectral image with spatial sampling related to $(\kappa_{\max} D)^{-1}$, the following computations assume that we are first able to upsample the spatial components of Eq. (40) to a finer spatial sampling related to $\Delta\alpha_{\min}$ in Eq. (32), corresponding to an upsampling factor of $|\mathbf{B}|_{\max} D^{-1}$. The image sampling has now been increased but the spatial resolution of the images remains unchanged.

The linear phase term associated with the spectral density in Eq. (40) is what will allow the collection of low-spatial-resolution measurements to eventually become a single high-spatial-resolution hyperspectral image because it relates the baseline to the spatial frequencies of the source. We can see this relationship between the interferometer baseline and the spatial frequencies of the source spectral density by taking the inverse Fourier transform from $\boldsymbol{\theta}$ to \mathbf{f}_θ of Eq. (40):

$$\begin{aligned} \tilde{S}_i(\mathbf{f}_\theta, \mathbf{B}; \kappa) &= \int_{-1}^1 S_i(\boldsymbol{\theta}, \mathbf{B}; \kappa) \exp(i2\pi\boldsymbol{\theta}\cdot\mathbf{f}_\theta) d^2\boldsymbol{\theta} \\ &= \pm i 2\Delta L_{\max} |\gamma_3|^2 \int_{-1}^1 \int_0^\infty \text{sinc}[2\Delta L_{\max}(\kappa - \kappa')] \\ &\quad \times \{ [S_s(\boldsymbol{\theta}; \kappa') \exp(i2\pi\kappa'\boldsymbol{\theta}\cdot\mathbf{B})] \overset{\theta}{*} p_{1,2}(\boldsymbol{\theta}; \kappa') \\ &\quad \times e^{i\Delta\varphi(\kappa')} \} \exp(i2\pi\boldsymbol{\theta}\cdot\mathbf{f}_\theta) d\kappa' d^2\boldsymbol{\theta} \\ &= \pm i 2\Delta L_{\max} |\gamma_3|^2 \int_{-1}^1 \int_0^\infty \text{sinc}[2\Delta L_{\max}(\kappa - \kappa')] \\ &\quad \times [\tilde{S}_s(\mathbf{f}_\theta - \kappa'\mathbf{B}; \kappa') \tilde{p}_{1,2}(\mathbf{f}_\theta; \kappa') e^{i\Delta\varphi(\kappa')}] d\kappa' \\ &= \pm i 2\Delta L_{\max} |\gamma_3|^2 \text{sinc}(2\Delta L_{\max}\kappa) \\ &\quad \times \{ \tilde{S}_s(\mathbf{f}_\theta - \kappa\mathbf{B}; \kappa) \tilde{p}_{1,2}(\mathbf{f}_\theta; \kappa) e^{i\Delta\varphi(\kappa)} \}, \end{aligned} \quad (41)$$

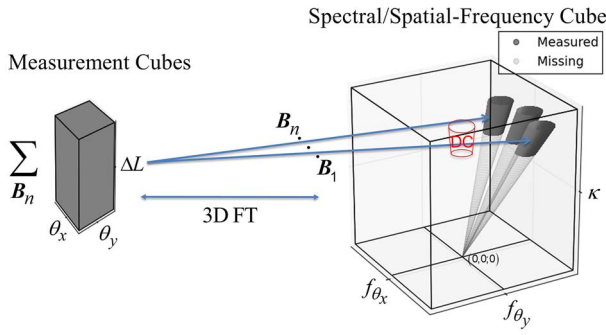


Fig. 2. Illustration of the information content probed by the datacube associated with each baseline vector. Each datacube maps out a truncated oblique cone in the spectral-spatial frequency domain whose location depends on the particular value of the baseline vector.

where

$$\tilde{p}_{1,2}(\mathbf{f}_\theta; \kappa) = \int_{-\infty}^{\infty} p_{1,2}(\boldsymbol{\theta}; \kappa) \exp(i2\pi\boldsymbol{\theta} \cdot \mathbf{f}_\theta) d^2\boldsymbol{\theta} \quad (42)$$

is the non-normalized SOTF of the system, and a tilde over a variable indicates a continuous Fourier transform from $\boldsymbol{\theta}$ to \mathbf{f}_θ . Equation (41) shows that the measurement cube for each baseline probes a different range of spatial frequencies, centered about $\mathbf{f}_\theta = \kappa\mathbf{B}$, of the source spectral density. The information content of a measurement cube for each baseline can be visualized as truncated oblique cones in a volume defined by \mathbf{f}_θ and κ , as seen in Fig. 2.

C. Image Processing and Effective Transfer Function

From Eq. (40), it is evident that there is another Fourier transform relationship between $\boldsymbol{\alpha}$ (or $\boldsymbol{\theta}$) and $\kappa\mathbf{B}$, which will provide a means of recovering a high-spatial-resolution hyperspectral image where the spatial resolution for the largest wavenumber is given by Eq. (32). This relationship, as well as the imaging properties of the system, is best understood through the effective transfer function of the interferometer system. Taking an inverse discrete Fourier transform (DFT) over the N_b baselines and exploiting the Fourier transform relationship between $\boldsymbol{\theta}$ and $\kappa\mathbf{B}$, we obtain the “dirty” high-resolution hyperspectral image:

$$\begin{aligned} S_i^{\text{hr}}(\boldsymbol{\theta}; \kappa) &= \sum_{n=1}^{N_b} S_i(\boldsymbol{\theta}, \mathbf{B}_n; \kappa) e^{i2\pi\boldsymbol{\theta} \cdot \mathbf{B}_n} \\ &= \pm i2\Delta L_{\text{max}} |\gamma_3|^2 \sum_{n=1}^{N_b} \left\{ \int_0^\infty \text{sinc}[2\Delta L_{\text{max}}(\kappa - \kappa')] \right. \\ &\quad \times \int_{-1}^1 S_s(\boldsymbol{\alpha}; \kappa') p_{1,2}(\boldsymbol{\theta} - \boldsymbol{\alpha}; \kappa') e^{i\Delta\varphi(\kappa')} \\ &\quad \left. \times \exp[i2\pi(\boldsymbol{\theta} - \boldsymbol{\alpha}) \cdot \mathbf{B}_n] d^2\boldsymbol{\alpha} d\kappa' \right\}. \end{aligned} \quad (43)$$

Substituting $\boldsymbol{\theta} - \boldsymbol{\alpha} = \boldsymbol{\theta}' + (\boldsymbol{\alpha} - \boldsymbol{\theta})$, we can rewrite Eq. (43) in the form of two convolutions:

$$\begin{aligned} S_i^{\text{hr}}(\boldsymbol{\theta}; \kappa) &= \pm i2\Delta L_{\text{max}} |\gamma_3|^2 \sum_{n=1}^{N_b} \left\{ \int_0^\infty \text{sinc}[2\Delta L_{\text{max}}(\kappa - \kappa')] \right. \\ &\quad \times \exp[i2\pi(\boldsymbol{\theta} - \boldsymbol{\alpha}') \cdot \mathbf{B}_n] \int_{-1}^1 S_s(\boldsymbol{\alpha}'; \kappa') e^{i\Delta\varphi(\kappa')} \\ &\quad \left. \times p_{1,2}(\boldsymbol{\theta} - \boldsymbol{\alpha}'; \kappa') \exp[i2\pi\boldsymbol{\theta}' \cdot \mathbf{B}_n] d^2\boldsymbol{\alpha}' d\kappa' \right\} \\ &= \pm i2\Delta L_{\text{max}} |\gamma_3|^2 \sum_{n=1}^{N_b} \left[\text{sinc}(2\Delta L_{\text{max}}\kappa) \right. \\ &\quad \times \exp(i2\pi\boldsymbol{\theta} \cdot \mathbf{B}_n)]^* \{ S_s(\boldsymbol{\theta}; \kappa) * [p_{1,2}(\boldsymbol{\theta}; \kappa) e^{i\Delta\varphi(\kappa)} \\ &\quad \times \exp(i2\pi\boldsymbol{\theta} \cdot \mathbf{B}_n)] \}. \end{aligned} \quad (44)$$

The linear phase term associated with the sinc wavenumber convolution kernel suggests that the delay line sampling for each baseline and point in the FOV should be centered about its associated ΔL_{ZPD} . In practice this means that ΔL_{max} must be large enough to capture $\pm|\Delta L_{\text{ZPD}}|_{\text{max}}$, as mentioned near the end of Section 3; fortunately, the ΔL_{max} needed to obtain the desired wavenumber resolution is typically large enough to satisfy this condition when compared with the largest baseline length and FOV that would be considered for astronomical imaging interferometry. The other linear phase term associated with the SPSF $p_{1,2}(\boldsymbol{\theta}; \kappa')$ is instead related to both the spatial frequency content associated with the baseline and the effective transfer function of the interferometer.

In order to obtain the effective transfer function, we compute the 2D spatial (angular) inverse Fourier transform of Eq. (44) using $\boldsymbol{\theta}$ and \mathbf{f}_θ as conjugate variables and employ the convolution theorem:

$$\begin{aligned} \tilde{S}_i^{\text{hr}}(\mathbf{f}_\theta; \kappa) &= \int_{-1}^1 S_i^{\text{hr}}(\boldsymbol{\theta}; \kappa) \exp(i2\pi\boldsymbol{\theta} \cdot \mathbf{f}_\theta) d^2\boldsymbol{\theta} \\ &= \pm i2\Delta L_{\text{max}} |\gamma_3|^2 \int_{-1}^1 \sum_{n=1}^{N_b} \int_0^\infty \text{sinc}[2\Delta L_{\text{max}}(\kappa - \kappa')] \\ &\quad \times \exp[i2\pi(\boldsymbol{\theta} - \boldsymbol{\alpha}') \cdot \mathbf{B}_n] \{ S_s(\boldsymbol{\theta}; \kappa) \\ &\quad * [p_{1,2}(\boldsymbol{\theta}; \kappa) e^{i\Delta\varphi(\kappa)} \exp(i2\pi\boldsymbol{\theta} \cdot \mathbf{B}_n)] \} \\ &\quad \times \exp(i2\pi\boldsymbol{\theta} \cdot \mathbf{f}_\theta) d\kappa' d^2\boldsymbol{\theta} \\ &= \pm i2\Delta L_{\text{max}} |\gamma_3|^2 \int_0^\infty \text{sinc}[2\Delta L_{\text{max}}(\kappa - \kappa')] \\ &\quad \times \sum_{n=1}^{N_b} \{ \tilde{S}_s[\mathbf{f}_\theta + (\kappa - \kappa')\mathbf{B}_n; \kappa'] \tilde{p}_{1,2}(\mathbf{f}_\theta + \kappa\mathbf{B}_n; \kappa') \} d\kappa'. \end{aligned} \quad (45)$$

The effective OTF of a double-Fourier interferometer is the summation of shifted SOTFs, where the shift, $\kappa\mathbf{B}_n$, is equal to the product of the baseline and wavenumber. This is most easily observed if we assume that the sinc convolution term in Eq. (45) is narrow enough to be approximated by a delta function, resulting in the following effective transfer function:

$$\text{OTF}_{\text{eff}}(\mathbf{f}_\theta; \kappa) \approx \sum_{n=1}^{N_b} \tilde{p}_{1,2}(\mathbf{f}_\theta + \kappa\mathbf{B}_n; \kappa). \quad (46)$$

We will return to the consequences of the above equation in Section 4.D to discuss imaging properties of the interferometer.

We can now relate Eqs. (41)–(45) through

$$\tilde{S}_i^{\text{hr}}(\mathbf{f}_\theta; \kappa) = \sum_{n=1}^{N_b} \tilde{S}_i(\mathbf{f}_\theta + \kappa \mathbf{B}_n, \mathbf{B}_n; \kappa), \quad (47)$$

which allows us to combine Eqs. (41) and (45)–(47) to create a new procedure for computing Eq. (44) from Eq. (40). We start by computing $\tilde{S}_i(\mathbf{f}_\theta, \mathbf{B}_n; \kappa)$, Eq. (41), for all baselines \mathbf{B}_n . We then apply Eq. (47) by shifting all $\tilde{S}_i(\mathbf{f}_\theta, \mathbf{B}_n; \kappa)$ by $\kappa \mathbf{B}_n$ before summing the results. Finally, we obtain the ultimate “dirty” high-resolution spectral image $S_i^{\text{hr}}(\boldsymbol{\theta}; \kappa)$ by taking the 2D Fourier transform of $\tilde{S}_i^{\text{hr}}(\mathbf{f}_\theta; \kappa)$ from \mathbf{f}_θ to $\boldsymbol{\theta}$. This procedure could possibly provide computational speed advantages if we consider that we can combine spatial upsampling with the computation of Eq. (41) instead of first upsampling Eq. (40) before the multiplications and summation of Eq. (43).

Note that the spectral density of the object is real valued, so its Fourier transform exhibits Hermitian symmetry, $\tilde{S}_i^{\text{hr}}(-\mathbf{f}_\theta; \kappa) = \tilde{S}_i^{\text{hr}*}(\mathbf{f}_\theta; \kappa)$, halving the number of spatial frequencies that must be measured. This just means that baselines \mathbf{B}_n and $-\mathbf{B}_n$ provide redundant information.

If we replace the “dirty” high-resolution hyperspectral image of Eq. (43) with a guess for the hyperspectral object being measured, the procedure for obtaining the “dirty” hyperspectral image can be reversed in order to simulate double-Fourier interferometric measurements in either the form of Eq. (26) or the bias-subtracted form of Eq. (37). Those simulations can be incorporated into a nonlinear optimization algorithm to recover the high-resolution hyperspectral image from a measurement set, allowing for the inclusion of regularization metrics to enforce prior knowledge of the object being measured. An inverse approach to image reconstruction has advantages that would mitigate issues associated with instrumental effects and inadequate sampling, which will be further discussed in Section 4.D. Simulations, such as those generated by the far-infrared interferometer instrument simulator [14], can be made to include many different instrumental effects, including, but not limited to, telescope pointing errors, background or detector noise, and thermal effects. Generating simulated measurements with instrumental effects, such as telescope pointing errors, provides a means for understanding the impact of instrumental errors on the quality of the hyperspectral image obtained after reconstruction [14].

D. Imaging Properties

The effective transfer function of the interferometer not only provides insight into the image reconstruction procedure but also into the system’s imaging properties, including the final image quality at each sampled wavenumber. Notice that the OTF in Eq. (46) is dependent on baseline sampling. This dependency indicates that different baseline separations probe different spatial frequencies in the source, and the effective OTF is then the sum of shifted versions of the SOTFs. Figure 2 illustrates this idea by showing that the information content of a measurement at a single baseline maps out a volume in the spectral-spatial frequency domain, which is a truncated oblique cone having a vertex at the (0,0,0) coordinate, and that each baseline vector corresponds to different portions of the object’s spectral-spatial frequencies. For this reason, baseline sampling is

chosen, time permitting, such that the volume describing the object’s spectral-spatial frequencies is populated without gaps. Furthermore, instead of simply summing components of the OTF, one would choose to weight them to arrive at a uniformly weighted effective transfer function. However, there are some spatial frequencies to which we do not have access without additional hardware.

Because it is physically impossible for the two apertures in a double-Fourier interferometer to coincide ($\mathbf{B}_n \neq 0$), the effective OTF must necessarily vanish at and around the DC spatial frequency, meaning that the lowest spatial frequencies are not measured, depicted in Fig. 2 by the empty volume traced in red. Without the low spatial frequency content, the recovered high-resolution images at each wavenumber will be zero-mean. However, conventional Fourier transform spectroscopy (FTS) is a means of recovering some of the missing information [9]. This could be achieved with an additional beam splitter, indicated by a thin line, and a mechanism to alter the interferometer configuration such that wide-field FTS is performed with a single aperture, as shown in Fig. 3, in addition to the double-Fourier measurements. If such increased system complexity is not an option, then we must find a way to estimate the low spatial frequencies that are not measured. A simple solution to this problem is to use the fringe bias from Eq. (36) to replace the low spatial frequencies. This is only an estimate because the fringe bias is a panchromatic image of the source, and this is equivalent to approximating the spectral density to be independent of wavenumber: $S_s(\boldsymbol{\alpha}, \kappa) \approx \psi g(\boldsymbol{\alpha})$. A more appropriate assumption would be a gray-world approximation for the spectral density, $S_s(\boldsymbol{\alpha}, \kappa) \approx \psi(\kappa)g(\boldsymbol{\alpha})$, which can be used to recover a more accurate estimate for the low spatial frequencies of the spectral image through the use of reconstruction algorithms [5].

Aside from missing spatial frequencies at and around the DC spatial frequency, there could be other missing spatial frequencies if the angular or radial collection of baselines is insufficient. Such sparsity in the spatial frequency domain will cause artifacts in the image domain that can be mitigated with regularization parameters, such as nonnegativity and L1-minimization, within the image reconstruction procedure. As mentioned above, the quality of the “dirty” image can be improved by appropriately weighting the spatial frequency content of $\tilde{S}_i^{\text{hr}}(\mathbf{f}_\theta; \kappa)$ provided that there are no gaps in spatial frequency coverage. Another option, which is particularly

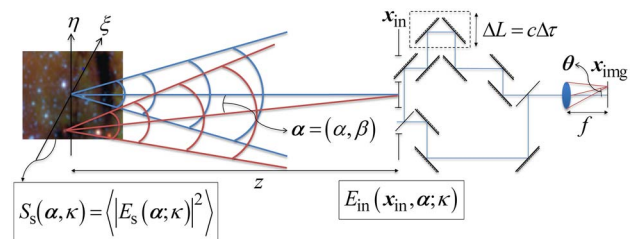


Fig. 3. Simplified diagram of a wide-field spatio-spectral interferometer an additional beam splitter and mirror to demonstrate that the same system can be used for conventional Fourier transform imaging spectroscopy.

important in the presence of missing spatial frequencies, is to use deconvolution techniques that have been developed for imaging interferometry such as CLEAN [15] or maximum entropy methods [16]. Some newer deconvolution methods are discussed by Thiébaud and Young [17] and have been tested in SPIE's *interferometric imaging beauty contest* [18].

Also, the system's effective OTF has a complicated geometry, related to that for Fizeau Fourier transform imaging spectroscopy [4,5], where the measured spatial frequencies scale with both baseline and wavelength, meaning that the spatial frequency content of each baseline measurement is slightly different for all wavelengths in the hyperspectral image. The effect of this Fourier geometry on image quality requires further investigation, but it is likely that similar image reconstruction and regularization techniques will be useful to mitigate artifacts in the resulting image.

5. CONCLUSION

A complete derivation of the measurement model for wide-field spatio-spectral interferometry based on Fresnel propagations and a two-aperture interferometer has been presented. This led to a generalization of the van Cittert–Zernike theorem that relates the spectral density of an incoherent source to the irradiance measured by the interferometer. We discussed delay line sampling in the context of desired spectral resolution as well as the impact of the delay line scan range on the spatial FOV of the interferometer. We also provided an estimate of the spatial (angular) resolution of an imaging interferometer based on the largest measured baseline length and wavenumber, but actual image quality and resolution are also dependent on baseline sampling and noise. A method for recovering a high-resolution hyperspectral image from a noiseless measurement set was derived. We made connections between baseline sampling and spectral OTF (SOTF) coverage and how they are related to imaging properties of the system through the interferometer's effective transfer function. Possible methods for overcoming the issue of missing low spatial frequencies, as well mitigating artifacts due to irregular baseline sampling, were proposed based on existing algorithms for imaging interferometry.

Future work will demonstrate the image reconstruction algorithm presented herein on simulated data as well as investigate the use of a regularized nonlinear optimization algorithm to recover an improved high-resolution hyperspectral image. We also intend to examine how lacking low spatial frequencies affects image synthesis and attempt recovery of low spatial frequencies without conventional wide-field FTS measurements.

APPENDIX A: RELATION TO COHERENCE THEORY

We begin by determining the intensities for each beam that would be measured if a large array detector were placed just before the beam splitter. The intensities of the individual beams before the beam splitter are found by taking the squared magnitude of Eq. (7) and applying Eq. (11), accounting for contributions from all field angles and wavelengths:

$$\begin{aligned} I_1(\mathbf{x}_{\text{pup}}) &= \left\langle \left| \int_0^\infty \int_{-1}^1 E_{1,\text{pup}}(\mathbf{x}_{\text{pup}}, \boldsymbol{\alpha}; \kappa) d^2\boldsymbol{\alpha} d\kappa \right|^2 \right\rangle \\ &= |\gamma_1|^2 \int_0^\infty |A_1(\mathbf{x}_{\text{pup}}; \kappa)|^2 \int_{-1}^1 \langle |E_s(\boldsymbol{\alpha}; \kappa)|^2 \rangle d^2\boldsymbol{\alpha} d\kappa, \end{aligned} \quad (\text{A1a})$$

$$I_2(\mathbf{x}_{\text{pup}}) = |\gamma_1|^2 \int_0^\infty |A_2(\mathbf{x}_{\text{pup}}; \kappa)|^2 \int_{-1}^1 \langle |E_s(\boldsymbol{\alpha}; \kappa)|^2 \rangle d^2\boldsymbol{\alpha} d\kappa. \quad (\text{A1b})$$

Without considering all field angles and wavelengths simultaneously, we would be implying assumptions about the coherence properties of the source field. We can, however, change the order of integration over time, angles, and wavenumber without loss of generality. Using Eqs. (7), (8), (11), and (A1), the measured intensities after the beam splitter for fixed delay $\Delta\tau$ are

$$\begin{aligned} I_3(\mathbf{x}_{\text{pup}}) &= \left\langle \left| \int_0^\infty \int_{-1}^1 E_{3,\text{pup}}(\mathbf{x}_{\text{pup}}, \boldsymbol{\alpha}; \kappa) d^2\boldsymbol{\alpha} d\kappa \right|^2 \right\rangle \\ &= \left\langle \left| \int_0^\infty \int_{-1}^1 [r_{\text{bs}} E_{1,\text{pup}}(\mathbf{x}_{\text{pup}}, \boldsymbol{\alpha}; \kappa) \right. \right. \\ &\quad \left. \left. + t_{\text{bs}} E_{2,\text{pup}}(\mathbf{x}_{\text{pup}}, \boldsymbol{\alpha}; \kappa)] d^2\boldsymbol{\alpha} d\kappa \right|^2 \right\rangle \\ &= RI_1(\mathbf{x}_{\text{pup}}) + TI_2(\mathbf{x}_{\text{pup}}) \\ &\quad + 2 \operatorname{Re} \left[r_{\text{bs}}^* t_{\text{bs}} \int_0^\infty \int_0^\infty \int_{-1}^1 \int_{-1}^1 \langle E_{1,\text{pup}}^*(\mathbf{x}_{\text{pup}}, \boldsymbol{\alpha}; \kappa) \right. \\ &\quad \left. \times E_{2,\text{pup}}(\mathbf{x}_{\text{pup}}, \boldsymbol{\alpha}'; \kappa') \rangle d^2\boldsymbol{\alpha}' d^2\boldsymbol{\alpha} d\kappa' d\kappa \right] \\ &= \frac{1}{2} [I_1(\mathbf{x}_{\text{pup}}) + I_2(\mathbf{x}_{\text{pup}})] \\ &\quad - \operatorname{Im} \left[\int_0^\infty \int_0^\infty \int_{-1}^1 \int_{-1}^1 \langle E_{1,\text{pup}}^*(\mathbf{x}_{\text{pup}}, \boldsymbol{\alpha}; \kappa) \right. \\ &\quad \left. \times E_{2,\text{pup}}(\mathbf{x}_{\text{pup}}, \boldsymbol{\alpha}'; \kappa') \rangle d^2\boldsymbol{\alpha}' d^2\boldsymbol{\alpha} d\kappa' d\kappa \right], \end{aligned} \quad (\text{A2a})$$

and similarly,

$$\begin{aligned} I_4(\mathbf{x}_{\text{pup}}) &= \frac{1}{2} [I_1(\mathbf{x}_{\text{pup}}) + I_2(\mathbf{x}_{\text{pup}})] \\ &\quad + \operatorname{Im} \left[\int_0^\infty \int_0^\infty \int_{-1}^1 \int_{-1}^1 \langle E_{1,\text{pup}}^*(\mathbf{x}_{\text{pup}}, \boldsymbol{\alpha}; \kappa) \right. \\ &\quad \left. \times E_{2,\text{pup}}(\mathbf{x}_{\text{pup}}, \boldsymbol{\alpha}'; \kappa') \rangle d^2\boldsymbol{\alpha}' d^2\boldsymbol{\alpha} d\kappa' d\kappa \right], \end{aligned} \quad (\text{A2b})$$

where the intensities from the output arms of the beam splitter, $I_{3,4}$, are implicitly functions of τ_1 , τ_2 , and \mathbf{B} . In the above equations, we applied the assumptions that $R = T = 1/2$ and that the phase difference between r_{bs} and t_{bs} is $\pi/2$. We also assume that the field is stationary in the wide sense, so that the interference term $\langle E_{1,\text{pup}}^* E_{2,\text{pup}} \rangle$ does not vary with integration start time t_a . Equations (A2a) and (A2b) can be combined into a single equation for the pupil intensity:

$$\begin{aligned}
I_{3,4}(\mathbf{x}_{\text{pup}}) &= \frac{1}{2}[I_1(\mathbf{x}_{\text{pup}}) + I_2(\mathbf{x}_{\text{pup}})] \\
&\mp \text{Im} \left[\int_0^\infty \int_0^\infty \int_{-1}^1 \int_{-1}^1 \langle E_{1,\text{pup}}^*(\mathbf{x}_{\text{pup}}, \boldsymbol{\alpha}; \kappa) \right. \\
&\quad \left. \times E_{2,\text{pup}}(\mathbf{x}_{\text{pup}}, \boldsymbol{\alpha}'; \kappa') \rangle d^2\boldsymbol{\alpha}' d^2\boldsymbol{\alpha} d\kappa' d\kappa \right]. \quad (\text{A3})
\end{aligned}$$

In order to further simplify the above equation, special attention must be paid to the integration of the cross term, which gives rise to an interference pattern that varies with induced time delay difference $\Delta\tau = \tau_2 - \tau_1$. Assume that $\Delta\tau$ and \mathbf{B} are fixed during a single measurement; then $\langle E_{1,\text{pup}}^* E_{2,\text{pup}} \rangle$ is a measure of the cross-spectral density, $W_{12}(\kappa)$, requiring that ([6], Section. 4.3.2)

$$\langle E_1^*(\boldsymbol{\alpha}) E_2(\boldsymbol{\alpha}') \rangle = W_{12}(\kappa) \delta(\boldsymbol{\alpha} - \boldsymbol{\alpha}'). \quad (\text{A4})$$

From the sifting property of the delta function, Eq. (A3) simplifies to

$$\begin{aligned}
I_{3,4}(\mathbf{x}_{\text{pup}}) &= \frac{1}{2}[I_1(\mathbf{x}_{\text{pup}}) + I_2(\mathbf{x}_{\text{pup}})] \\
&\mp \text{Im} \left[\int_0^\infty W_{12}^{\text{pup}}(\mathbf{x}_{\text{pup}}, \kappa) d\kappa \right], \quad (\text{A5})
\end{aligned}$$

where

$$\begin{aligned}
W_{12}^{\text{pup}}(\mathbf{x}_{\text{pup}}, \kappa) &= \int_{-1}^1 \int_{-1}^1 \langle E_{1,\text{pup}}^*(\mathbf{x}_{\text{pup}}, \boldsymbol{\alpha}; \kappa) \\
&\quad \times E_{2,\text{pup}}(\mathbf{x}_{\text{pup}}, \boldsymbol{\alpha}'; \kappa) \rangle d^2\boldsymbol{\alpha}' d^2\boldsymbol{\alpha} \quad (\text{A6})
\end{aligned}$$

is a measure of cross-spectral density in the interferometer's exit pupil. Combining Eqs. (7) and (A6), we have

$$\begin{aligned}
&W_{12}^{\text{pup}}(\mathbf{x}_{\text{pup}}, \kappa) \\
&= |\gamma_1|^2 \int_{-1}^1 \int_{-1}^1 \left\langle e^{i\Delta\varphi(\kappa)} e^{-i2\pi\kappa[z-c(t+\tau_1)]} \exp \left[-i\pi\frac{\kappa}{z} \left(\mathbf{x}_{\text{pup}} + \frac{1}{2}\mathbf{B} \right)^2 \right] \right. \\
&\quad \times E_s^*(\boldsymbol{\alpha}; \kappa) A_1^*(\mathbf{x}_{\text{pup}}; \kappa) e^{-i\pi\kappa\alpha^2} \exp \left[-i2\pi\kappa\boldsymbol{\alpha} \cdot \left(\mathbf{x}_{\text{pup}} + \frac{1}{2}\mathbf{B} \right) \right] \\
&\quad \times e^{i2\pi\kappa[z-c(t+\tau_2)]} \exp \left[i\pi\frac{\kappa}{z} \left(\mathbf{x}_{\text{pup}} - \frac{1}{2}\mathbf{B} \right)^2 \right] E_s(\boldsymbol{\alpha}'; \kappa) \\
&\quad \left. \times A_2(\mathbf{x}_{\text{pup}}; \kappa) e^{i\pi\kappa\alpha'^2} \exp \left[i2\pi\kappa\boldsymbol{\alpha}' \cdot \left(\mathbf{x}_{\text{pup}} - \frac{1}{2}\mathbf{B} \right) \right] \right\rangle d^2\boldsymbol{\alpha}' d^2\boldsymbol{\alpha} \\
&= |\gamma_1|^2 \int_{-1}^1 \int_{-1}^1 e^{i\Delta\varphi(\kappa)} e^{-i2\pi\kappa c\Delta\tau} \exp \left(-i2\pi\frac{\kappa}{z} \mathbf{x}_{\text{pup}} \cdot \mathbf{B} \right) \\
&\quad \times \langle E_s^*(\boldsymbol{\alpha}; \kappa) E_s(\boldsymbol{\alpha}'; \kappa) \rangle A_1^*(\mathbf{x}_{\text{pup}}; \kappa) A_2(\mathbf{x}_{\text{pup}}; \kappa) \\
&\quad \times \exp[i\pi\kappa z(\boldsymbol{\alpha}'^2 - \boldsymbol{\alpha}^2)] \\
&\quad \times \exp\{-i\pi\kappa[(\boldsymbol{\alpha} + \boldsymbol{\alpha}') \cdot \mathbf{B} - 2(\boldsymbol{\alpha}' - \boldsymbol{\alpha}) \cdot \mathbf{x}_{\text{pup}}]\} d^2\boldsymbol{\alpha}' d^2\boldsymbol{\alpha}. \quad (\text{A7})
\end{aligned}$$

We can simplify further by recalling, again, that the astronomical source is assumed to be spatially incoherent, which is mathematically expressed as

$$\begin{aligned}
\langle E_s^*(\boldsymbol{\alpha}; \kappa) E_s(\boldsymbol{\alpha}'; \kappa') \rangle &= W_s(\boldsymbol{\alpha}, \boldsymbol{\alpha}'; \kappa) \delta(\kappa - \kappa') \\
&\propto \sigma S_s(\boldsymbol{\alpha}; \kappa) \delta(\boldsymbol{\alpha} - \boldsymbol{\alpha}', \kappa - \kappa'). \quad (\text{A8})
\end{aligned}$$

Similarly, the spectral density for an incoherent source obeys

$$\langle |E_s(\boldsymbol{\alpha}; \kappa)|^2 \rangle \propto \sigma S_s(\boldsymbol{\alpha}; \kappa). \quad (\text{A9})$$

Using Eqs. (A8) and (A9), we can further simplify Eqs. (A1) and (A7), integrating over $\boldsymbol{\alpha}'$ when needed:

$$I_1(\mathbf{x}_{\text{pup}}) = |\gamma_4|^2 \int_0^\infty |A_1(\mathbf{x}_{\text{pup}}; \kappa)|^2 \int_{-1}^1 S_s(\boldsymbol{\alpha}; \kappa) d^2\boldsymbol{\alpha} d\kappa, \quad (\text{A10a})$$

$$I_2(\mathbf{x}_{\text{pup}}) = |\gamma_4|^2 \int_0^\infty |A_2(\mathbf{x}_{\text{pup}}; \kappa)|^2 \int_{-1}^1 S_s(\boldsymbol{\alpha}; \kappa) d^2\boldsymbol{\alpha} d\kappa, \quad (\text{A10b})$$

and

$$\begin{aligned}
W_{12}^{\text{pup}}(\mathbf{x}_{\text{pup}}, \kappa) &= |\gamma_4|^2 \int_{-1}^1 e^{i\Delta\varphi(\kappa)} e^{-i2\pi\kappa c\Delta\tau} A_1^*(\mathbf{x}_{\text{pup}}; \kappa) A_2(\mathbf{x}_{\text{pup}}; \kappa) \\
&\quad \times \exp \left(-i2\pi\frac{\kappa}{z} \mathbf{x}_{\text{pup}} \cdot \mathbf{B} \right) W_{12}^{\text{in}}(\boldsymbol{\alpha}; \kappa) d^2\boldsymbol{\alpha}, \quad (\text{A11})
\end{aligned}$$

where

$$W_{12}^{\text{in}}(\boldsymbol{\alpha}; \kappa) = S_s(\boldsymbol{\alpha}; \kappa) e^{-i2\pi\kappa\boldsymbol{\alpha} \cdot \mathbf{B}}, \quad (\text{A12})$$

and

$$\gamma_4 = \gamma_1 \sigma^{1/2} = \frac{iz}{\pi^{1/2} \kappa^2}. \quad (\text{A13})$$

$W_{12}^{\text{in}}(\boldsymbol{\alpha}; \kappa)$ is the cross-spectral density of the field in the entrance pupil plane of the interferometer due to a point object at $\boldsymbol{\alpha}$. Equation (A12) has a special functional form arising from the far-field propagation of an incoherent source that shows the cross-spectral purity of the field in the pupil plane. Namely, the fields at each aperture have identical spectral densities, and the combined field from both apertures has the same spectral density as the individual fields ([6], Section 4.5.1; [8], Section 5.3.2; [19]). Equation (A6) can only be related to the mutual coherence function, $\Gamma(-\mathbf{B}/2, \mathbf{B}/2, \Delta\tau) = \Gamma(\mathbf{B}, \Delta\tau) = \Gamma_{12}(\Delta\tau)$, in the pupil plane if $\Delta\varphi$, A_1 , and A_2 are all independent of wavenumber, including phase aberrations, which is an idealized assumption that depends on characteristics of the interferometer ([6], Section 4.3.2; [8], Section 5.2.5). In general, the mutual coherence function and the cross-spectral density are related through the Wiener–Khintchine theorem ([6], Section 4.3.2; [8], Section 3.4.2), which becomes apparent after integration over all κ :

$$\Gamma_{12}(\tau) = \int_0^\infty W_{12}(\nu) e^{-i2\pi\nu\tau} d\nu = c \int_0^\infty W_{12}(\kappa) e^{-i2\pi\kappa c\tau} d\kappa. \quad (\text{A14})$$

We will now incorporate the preceding assumptions for the time being for the sole purpose of making a clear connection between the intensity in the exit pupil of the interferometer and the mutual coherence function through application of the Wiener–Khintchine theorem:

$$\begin{aligned}
& I_{3,4}(\mathbf{x}_{\text{pup}}) \\
&= \frac{1}{2} [I_1(\mathbf{x}_{\text{pup}}) + I_2(\mathbf{x}_{\text{pup}})] \mp c^{-1} |\gamma_4|^2 \text{Im} \left\{ e^{i\Delta\varphi} A_1^*(\mathbf{x}_{\text{pup}}) A_2(\mathbf{x}_{\text{pup}}) \right. \\
&\quad \times \int_{-1}^1 c \int_0^\infty \exp \left[-i2\pi c \kappa \left(\Delta\tau + \frac{\mathbf{x}_{\text{pup}} \cdot \mathbf{B}}{cz} \right) \right] W_{12}^{\text{in}}(\boldsymbol{\alpha}, \kappa) d\kappa d^2\boldsymbol{\alpha} \left. \right\} \\
&= \frac{1}{2} [I_1(\mathbf{x}_{\text{pup}}) + I_2(\mathbf{x}_{\text{pup}})] \mp c^{-1} |\gamma_4|^2 \text{Im} \left[e^{i\Delta\varphi} A_1^*(\mathbf{x}_{\text{pup}}) A_2(\mathbf{x}_{\text{pup}}) \right. \\
&\quad \times \left. \int_{-1}^1 \Gamma_{12}^{\text{in}} \left(\boldsymbol{\alpha}, \Delta\tau + \frac{\mathbf{x}_{\text{pup}} \cdot \mathbf{B}}{cz} \right) d^2\boldsymbol{\alpha} \right], \quad (\text{A15})
\end{aligned}$$

where $\Gamma_{12}^{\text{in}}(\boldsymbol{\alpha}; \Delta\tau)$ is the mutual coherence in the entrance pupil of the interferometer for each source angle and position in the pupil. The above equation offers insight into the physical quantities being probed by double-Fourier interferometry. In the most general sense, this technique makes measurements of both spatial and temporal coherence in the entrance pupil through the mutual coherence function. This is ultimately a generalization of the van Cittert–Zernike theorem, which exploits the propagation of mutual intensity from an incoherent source; instead, double-Fourier interferometry exploits the propagation of the more general mutual coherence function. Although we had assumed that $\Delta\varphi$, A_1 , and A_2 were independent of wavelength, we could have relaxed this assumption and the intensity in the exit pupil of the interferometer would still be related to the mutual coherence function in the interferometer's entrance pupil with additional convolution kernels that depend on the path difference $\Delta\tau$. The convolutions imparted by the spectral variations in the complex-valued aperture functions can be calibrated out of the measurements during post-processing if they are measured or known *a priori*. Analogous to the van Cittert–Zernike theorem, the intensity in the interferometer's exit pupil can also be related directly to the source spectral density. For this purpose, we return to the more general case where spectral variations exist and combine Eqs. (A5), (A11), and (A12):

$$\begin{aligned}
I_{3,4}(\mathbf{x}_{\text{pup}}) &= \frac{1}{2} [I_1(\mathbf{x}_{\text{pup}}) + I_2(\mathbf{x}_{\text{pup}})] \\
&\quad \mp |\gamma_4|^2 \text{Im} \left\{ \int_{-1}^1 \int_0^\infty e^{i\Delta\varphi(\kappa)} A_1^*(\mathbf{x}_{\text{pup}}, \kappa) A_2(\mathbf{x}_{\text{pup}}, \kappa) \right. \\
&\quad \times \exp \left[-i2\pi c \kappa \left(\Delta\tau + \frac{\mathbf{x}_{\text{pup}} \cdot \mathbf{B}}{cz} + \frac{\boldsymbol{\alpha} \cdot \mathbf{B}}{c} \right) \right] \\
&\quad \times \left. S_s(\boldsymbol{\alpha}; \kappa) d\kappa d^2\boldsymbol{\alpha} \right\}. \quad (\text{A16})
\end{aligned}$$

The linear phase term proportional to $\mathbf{x}_{\text{pup}} \cdot \mathbf{B}$ can be dropped for astronomical distances as well as for meticulously designed lab experiments, as long as Eq. (22) is satisfied. The remaining phase terms proportional to $\kappa\Delta\tau$ and $\kappa\boldsymbol{\alpha} \cdot \mathbf{B}$ are the necessary terms required for conventional FTS and Michelson stellar interferometry, respectively. Conventional spatio-spectral interferometry, as discussed by Mariotti and Ridgway [[9], Eq. (6)] for example, would stop here and place a large bucket detector after the beam splitter. One would typically simplify Eq. (A16) even more by making further idealizations (identical

apertures and aberrations, etc.) about the system in order to obtain better insight into how different source spectral densities will be manifested in the measurements. Such a measurement regime provides a limited FOV and has demanding baseline sampling requirements in order to form a hyperspectral image from the measurements. Instead, a wide FOV extension to spatio-spectral interferometry has been developed [1–3], as described in Section 2.B.

Funding. NASA Space Technology Research Fellowship (NNX14AL73H).

REFERENCES

1. R. G. Lyon, S. A. Rinehart, D. T. Leisawitz, and N. Memarsadeghi, "Wide-field imaging interferometry testbed (WIIT): image construction algorithms," Proc. SPIE **7013**, 70131M (2008).
2. R. G. Lyon, D. T. Leisawitz, S. A. Rinehart, N. Memarsadeghi, and E. J. Sinukoff, "Wide-field imaging interferometry spatial-spectral image synthesis algorithms," Proc. SPIE **8445**, 84450B (2012).
3. N. Elias, M. Harwit, D. T. Leisawitz, and S. A. Rinehart, "The mathematics of double-Fourier interferometers," Astrophys. J. **657**, 1178–1200 (2007).
4. S. T. Thurman and J. R. Fienup, "Multi-aperture Fourier transform imaging spectroscopy: theory and imaging properties," Opt. Express **13**, 2160–2175 (2005).
5. S. T. Thurman and J. R. Fienup, "Fizeau Fourier transform imaging spectroscopy: missing data reconstruction," Opt. Express **16**, 6631–6645 (2008).
6. L. Mandel and E. Wolf, *Optical Coherence and Quantum Optics* (Cambridge University, 1995).
7. A. Zeilinger, "General properties of lossless beam splitters in interferometry," Am. J. Phys. **49**, 882–883 (1981).
8. J. W. Goodman, *Statistical Optics*, 2nd ed. (Wiley, 2000).
9. J.-M. Mariotti and S. T. Ridgway, "Double Fourier spatio-spectral interferometry—combining high spectral and high spatial resolution in the near infrared," Astron. Astrophys. **195**, 350–363 (1988).
10. S. T. Thurman and J. R. Fienup, "Dealiased spectral images from aliased Fizeau Fourier transform spectroscopy measurements," J. Opt. Soc. Am. A **24**, 68–73 (2007).
11. D. B. Leviton, B. J. Frey, D. T. Leisawitz, A. J. Martino, W. L. Maynard, L. G. Mundy, S. A. Rinehart, S. H. Teng, and X. Zhang, "Wide-field imaging interferometry testbed 3: metrology subsystem," Proc. SPIE **4852**, 827–838 (2003).
12. S. T. Thurman and J. R. Fienup, "Signal-to-noise ratio trade-offs associated with coarsely sampled Fourier transform spectroscopy," J. Opt. Soc. Am. A **24**, 2817–2821 (2007).
13. J. D. Monnier, "Optical interferometry in astronomy," Rep. Prog. Phys. **66**, 789–857 (2003).
14. R. Juanola-Parramon, D. M. Fenech, and G. Savini, "Architecture and performance of the space-based far-infrared interferometer instrument simulator," Mon. Not. R. Astron. Soc. **457**, 3457–3469 (2016).
15. J. A. Högbom, "Aperture synthesis with a non-regular distribution of interferometer baselines," Astron. Astrophys. **15**, 417–426 (1974).
16. R. Narayan and R. Nityananda, "Maximum entropy image restoration in astronomy," Annu. Rev. Astron. Astrophys. **24**, 127–170 (1986).
17. E. Thiébaud and J. Young, "Principles of Image reconstruction in optical interferometry: tutorial," J. Opt. Soc. Am. A **34**, 904–923 (2017).
18. J. Sanchez-Bermudez, E. Thiébaud, K.-H. Hofmann, M. Heining, D. Schertl, G. Weigelt, F. Millour, A. Schutz, A. Ferrari, M. Vannier, D. Mary, and J. Young, "The 2016 interferometric imaging beauty contest," Proc. SPIE **9907**, 99071D (2016).
19. L. Mandel, "Concepts of cross-spectral purity in coherence theory," J. Opt. Soc. Am. **51**, 1342–1350 (1961).